Gravity driven particle-laden flow

Sarah Burnett, Andrew Li, Matthew Molinare, Katherine Varela

August 15, 2014

Abstract

We present new experimental and theoretical results for the resuspension of mono- and bidisperse particle-laden flows on an inclined plane. In particular, we study the case of two negatively buoyant particle species of similar size and dissimilar densities in a viscous fluid of finite volume. Different regimes of particle separation are observed and studied by adjusting the angle of inclination, total particle concentration, and relative particle volume ratio. In addition to obtaining information about the height profile of shock formations, we measure the advancement and separation of particle and fluid front positions in mono- and bidisperse scenarios. We also propose a new theory for the transient state with good agreement in power law relations with volume and particle diameters. These dynamics are the basis for a quantitative understanding of polydisperse cases, which can be readily applied to industry and catastrophe modeling.

Contents

1 Theory

The subject of particle laden flow includes many physical phenomena. The simplest case of clear fluid flowing down an incline was first explored by Huppert [1], who found that the clear fluid front was related to time by the expression

$$x(t) = Ct^{1/3}$$

where C is some prefactor. The phenomenon of particle laden flow can therefore be considered as a natural extension from this case. The particular type of experimental setup of this research allows certain equations to be simplified, while introducing new dominant effects and approximations. Of most interest are the reduction of Navier-Stokes equation, and the consideration of shear induced migration.

The Navier-Stokes equation can be reduced to the Stokes equation for systems with high viscosity such that the Reynolds number becomes very small. This is done by keeping only the viscous terms and removing all the inertial terms:

$$-\nabla \cdot (-P\mathbb{I} + \mu(\phi)(\nabla \mathbf{u} + \nabla \mathbf{u}^T)) = (\rho_p \phi + \rho_\ell (1-\phi))\mathbf{g}$$

This is a reasonable reduction for the experiments since the fluid used in our experiment has an effective viscosity of 1000cSt.

On the other hand, the effects of shear-induced migration must be taken into account for such viscous mixtures. First observed in Couette flows, this phenomenon describes why and how particles that sink in a viscous fluid migrate due to viscous forces. We approach this phenomenon as a result of irreversible inter-particle interactions as proposed by Leighton and Acrivosesearch [2].

The flow of particle slurries is governed by a system of first order hyperbolic transport equations (h the total height, h_i the height of particle species i, ϕ_i the volume fraction of each particle species, and n_i the number density of the particle.

$$\begin{gathered}
\phi_i = \tfrac{n_i}{h} \\
\partial_t h + \nabla \cdot \left(h^3 F\left(\phi_1, \phi_2\right)\right) = 0 \\
\partial_t n_1 + \nabla \cdot \left(h^3 G_1\left(\phi_1, \phi_2\right)\right) = 0 \\
\partial_t n_2 + \nabla \cdot \left(h^3 G_1\left(\phi_1, \phi_2\right)\right) = 0
\end{gathered}$$

2 Experimental Procedure

2.1 General Setup

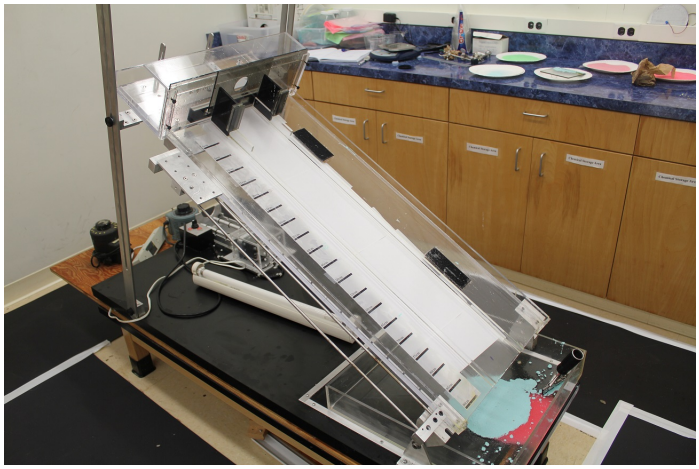

Figure 1: Basic Setup

The experiments make use of an inclined surface, different particle species, and silicone oil. Adjustable parameters include the angle (α), volume (V), diameter (d), and volume fraction of particles (ϕ). In the specific case of bidisperse experiments, an additional parameter λ, defined as the ratio of lighter particle volume fraction over total particle volume fraction, can be adjusted as well.

For all experiments, the x-axis is defined along the slope, the z-axis perpendicular to the slope, and mixture movement is approximately uniform with respect to the y-axis, the direction perpendicular to the two side walls of the track.

There are two particle species, ceramic (SLZ), and glass (GSB), both produced by CeroGlass. For each particle species three different diameter sizes were used. Smaller diameter sizes must be used for smaller volumes in order to conserve the assumption of continuum mechanics

$$\left(\frac{d}{H}\right)^2 \ll 1$$

where H is the fluid height. The silicone oil used in the particle slurries was the 1000cSt silicone oil. However, 100cSt silicone oil was used for prelayering as it appeared to reduce the fingering instabilities more effectively. Other silicone oils of varying viscosity are also present in small amounts in the laboratory's chemical storage units.

The laboratory has a Class II laser sheet pointer and Z-Light sphere (Type G-1350) for height profile measurement, and a set of black lights for fluorescent experiments. One should be cautious when using the Z-light spheres as they are very small and

can become suspended in air and inhaled.

2.2 Particle Dyeing

Ceramic beads are initially white in color, and can be dyed with food coloring. To provide a sharp constrant for data processing of bidisperse front tracking experiments, ceramic particles were dyed blue and glass particles were dyed red. For the ceramic dye, approximately 20 drops of food coloring was used for every 400g of particles. The particles were placed in a clean Zip-Lock bag, which was then sealed and thoroughly mixed until the color appeared uniform.

When a darker color is desired, one may add more dye as necessary. The process for fluorescent dying is described in Section 2.6. Particle clumping can result in a nonuniform distribution of particles that affect the particle concentration and behavior, most noticeably at the front in the ridged cases. This issue can be resolved by leaving the particles spread out in a paper plate for a day and mixing/grinding them in another clean Zip-Lock bag till no observable clumps are remaining. If there is insufficient time to let the particles dry, one can also heat the particles in the laboratory microwave to increase the rate of evaporation. No noticeable difference was observed by using these two methods this year.

GSB particles are transparent, and can be dyed with acrylic paint. As mentioned above, the GSB color was chosen to be red. To dye 400g of GSB particles red, 5mL of acrylic paint and 5mL of water were added into a beaker and thoroughly stirred. The mixture was then poured into a Zip-Lock bag with the particles and followed the same procedure used for drying ceramic particles.

2.3 Prelayering

To avoid the complications of contact line physics and reduce instabilities such as viscous fingers at the fluid front, the track was prelayered with a thin layer of silicone oil for each experiment. It was observed that fingering reduced further by using a lower density silicone oil(100Cst), which was adopted as the standard protocol for prelayering.

To prelayer the surface, a small amount of 100cSt oil should be poured slightly behind the gate. A squeegee was then used to wipe the excess fluid off the incline. There should not be any obvious streaks of fluid or particles remnants. While cleaning, one must be especially thorough with the boundaries, checking for residual fluid. This is necessary to prevent oil from running off along the boundaries, causing the front position to stagnate and creating complications for image processing. Ideally, the fluid should only lag behind slightly at the boundaries.

An initial attempt used to prelayer the surface was to pour fluid down the slope and leave it overnight to run off the track and become uniformly thin. Apart from the expensiveness of the process (only usable once per day), this method was abandoned as individual particles hidden along the boundaries and up along the slope migrate to cause irregularities on the thin film.

2.4 Mixing and Volume Procedures

Plastic cups were used to contain the particles and fluid. The typical volume loss for each trial was about 20 percent. Volume loss becomes increasingly serious as particle concentration increases. To compensate for this issue, one can increase the initial volume by approximately the average volume loss per trial. Since the particles are poured into the fluid for mixing, one can approximate the loss of particles due to electrostatic forces (minimal) by zeroing the mass of cups after pouring some particles in and then out.

After pouring the particles into the fluid, a plastic utensil was used to stir the mixture. The suspension should be initially well-mixed and left to sit for 10 minutes to remove large air bubbles. Approximately 2 minutes before the experiment starts, one should start stirring the mixture until well-mixed. While small air bubbles are unavoidable, the total volume of such bubbles and size can be reduced by stirring without breaking the surface of mixture [4]. This becomes more difficult as the particle concentration increases. It is best to pour the mixture into the resevoir behind the gate immediately to reduce the effects of particles settling in the unperturbed mixture.

2.5 Monodisperse and Bidisperse Experiment

Relative particle ratios (λ) of 0.25, 0.5, and 0.75 were attempted in bidisperse experiments using glass and ceramic particles. Since post-processing worked best in 50-50 cases where the contrast of the two particle species was the sharpest, more experiments were conducted at $\lambda = 0.5$

Certain limitations prevents us from gathering a full range of concentration data. As particle concentration increases, the effective viscosity of the mixture becomes higher, resulting in longer experimental time. At lower angles (settled regime), the particle front becomes settled at a shorter distances, which one would need to adjust the camera to capture. At larger angles (ridged regime), as particles aggregate to the front, higher concentrations can cause the front to break apart, causing chunks of particles to slide down the slope. This was frequently observed after 50cm.

Figure 2: Irregular clumps at breaking point

Breaking occurs more readily are larger concentrations and angles, so experiments were conducted generally with ϕ less than 0.5, and α less than 50 degrees.

2.6 Fluorescent Experiment

Careful procedures must be carried out in our experimental setup to ensure the calibrations function properly. To begin, the particle must be dyed with the fluorescent paint. The dye consists of 10 mL of paint and 30 mL of water. We mix this with 900 g of particles inside a sealed Ziploc bag and lay them out to dry on a paper plate. Typically this ratio works best for our smallest glass particles, GSB9. Less paint may be used for larger particles to avoid clumping. Red and green paints are preferred for data analysis so that we can reduce the intensity measurement to those particular color channels and reduce noise from the blue channel caused by the black lights.

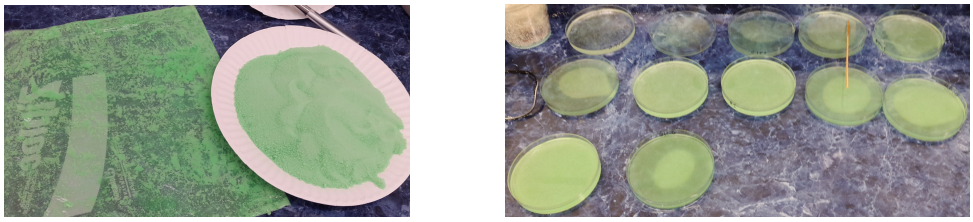

Figure 3: Left: Dyed particles. Right: Samples of varied particle mass.

Once the particles have dried, two calibrations must be set up. The first calibration is used in order to establish the relation between intensity and number density. Next, we measure the appropriate particle and fluid mass when the total volume is 30mL, the amount required to fill a Petri dish. The first sample should start with 1 g of particles, and for each consecutive sample increase by 1.5 g for a total of 12 sample. Higher amounts of particles result in intensity saturation and are not useful for the calibration. After thorough mixing, we place the sample in the center of the flat

track ($\alpha = 0$) and secure the black lights. We are careful in recording the x-position of the sample as well as the distance to the sample from the camera lens. The camera should be adjusted so that the sample appears at the center mark. In mode 'M', the following camera parameters are necessary to keep constant for all fluorescent shots: neutral picture style, disabled light optimizer, white balance: 3500K, aperture f/5.6, shutter speed 1/25, ISO 800, manual focus set. Any changes in these parameters can alter the intensity observed in the experiment and result in bad data. Furthermore, it is essential for later post-processing that we measure the volume of particles in each sample.

Figure 4: Density to intensity calibration setup.

After the experiment is run, we perform a position calibration to find change in intensity as a function of x-position. Running the experiment is very similar to running the normal experiments with pre-layering and mixing alike. However, the distance of the camera to the inclined track must be the same as the first calibration and the focus mark must be place at the same location as the samples. With the same camera parameters set, we set the intervalometer to take photos every 3 seconds. The first few photos should be taken with the lights on the get the centimeter position measurements on the side of the track. After the lights are turned off, the experiment can be run as usual, continuing the interval shooting. Once the experiment is over and the track is clean, the position calibration must be taken without changing the placement of the camera or the incline. We create a sample in a petri dish that matches the particle density of one of the samples from the first calibration. A preferable one is 10 g which should be mixed with a small amount of 10,000 cSt silicon oil. This highly viscous oil will temporarily keep the particles in place in the dish when it is placed on the incline. Three people are needed for this calibration. The first person places the sample on the incline starting centered at 0 cm and moves from 10 to 70 cm at 5 cm intervals. A second person is need to prop the sample with a stick so that it does not slide down the incline. The third person is responsible for operating the camera.

After this calibration is established using the calibration code, the experimental data is ready to be processed.

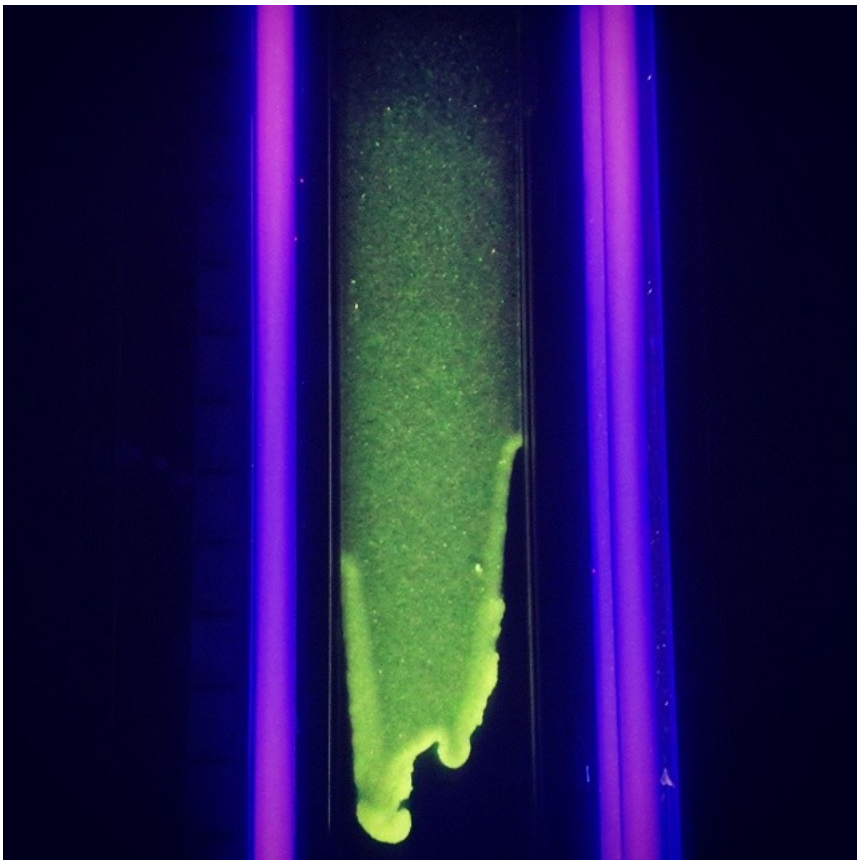

Figure 5: Yellow Intensity Experiment

Figure 6: Position to intensity calibration.

2.7 Height Profile

The primary instrument used to extract height profile measurements is a Class II laser fitted with a cylindrical lens. This optic device fans the beam to a plane of non-negligible thickness ($\approx 1\,mm$). We align the laser sheet so that the incident beam is normal to the slurry surface (see Fig. 7). A mounted Canon EOS Rebel T2i camera captures a video of the slurry as it advances down the incline. The camera is positioned at a slight offset to the side of the track in order to detect the entire shock formation. Previous attempts to measure the height profile were unsuccessful at capturing the front portion of the shock that, without this perspective change, is obscured by its own shadow. To improve resolution, we conduct our experiments in the dark and increase the camera's light sensitivity to ISO 1600. An f/10.3 aperture is used to widen the depth of field and ensure the entire track is in focus.

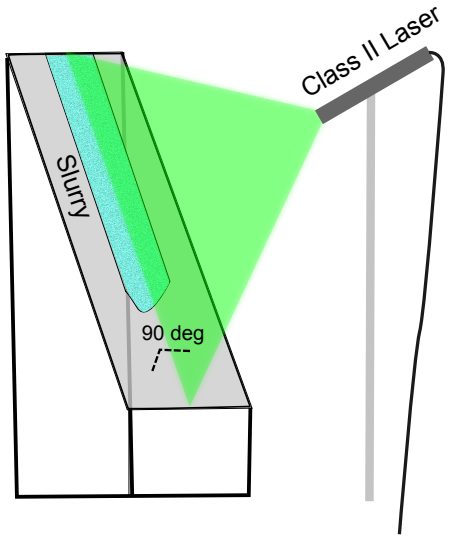

Figure 7: Laser sheet experimental setup; incident beam is normal to track surface.

We perform a series of calibration steps in our experimental procedure to obtain reliable data for the time-evolution of the height profile. Fine G-1350 particles (55 microns in diameter) and a sieve (of mesh size 150 microns) are used to deposit a thin layer on the track surface. These powder-like particles reflect the laser beam and provide a sharp baseline for the height that is useful in post-processing. A long ribbon with markings every $5\,cm$ is placed along the center of the track to rescale the length-axis of our images from pixels to centimeters. We cannot use the track's existing ruler because of the low camera angle from which we record our data. Furthermore, we need a method that will convert the slurry height in each column of our image from pixels to centimeters while correcting for the cameras perspective offset. This is accomplished by taking a picture of the height profile of a ruler of known and uniform height (Figure 8). Because the thickness of the ruler is comparable to the height of the slurry ($\approx 5\,mm$), we can reasonably negate any effects due to lens distortion.

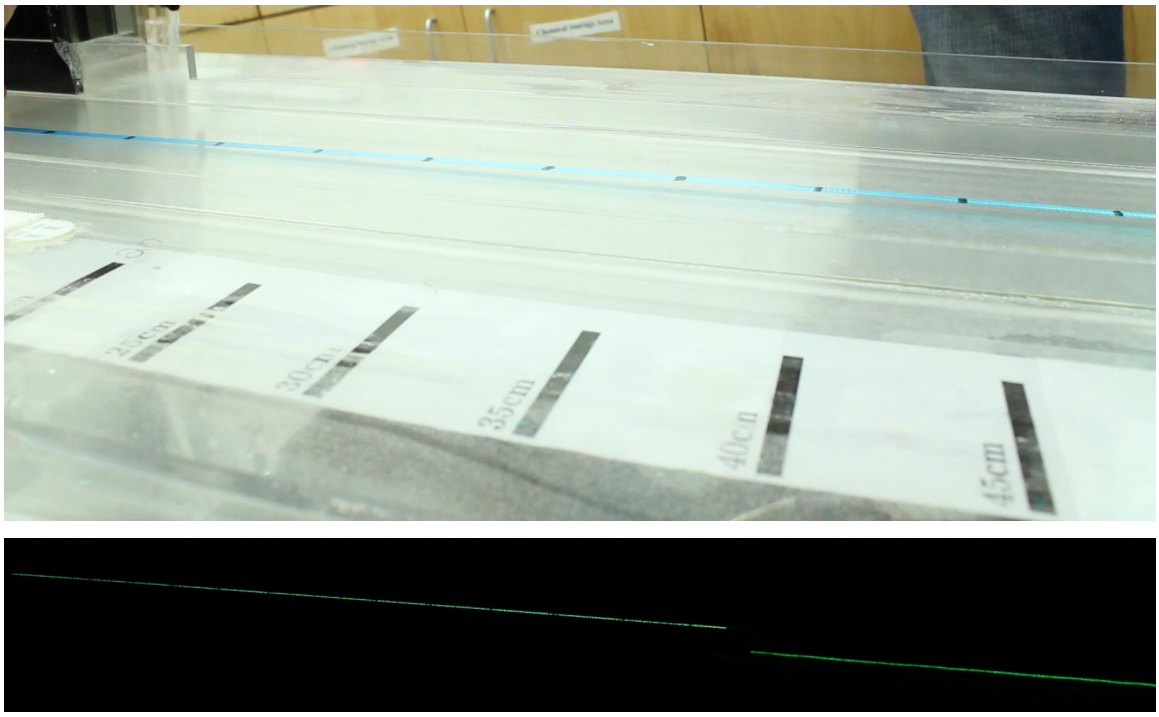

Figure 8: Top: Ribbon calibration setup. User inputs position of black markings. Bottom: Laser profile of ruler used in perspective correction.

These methods are viable for particle-laden flows in the ridged and well-mixed regimes, where the topmost particles are indistinguishable from the surface of the slurry. This is not case, however, in settled flows, where the transparent fluid separates from the particles. In this regime, we expect to observe a particle shock that lags behind a fluid shock. As before, we lightly coat the slurry with the G-1350 (powdering) particles (Fig. 9). A comparison of the measured height for a ridged case before and directly after the application of this coat revealed that the thickness of the powder is negligible. For ridged and well-mixed flows, we are able to capture a large number of frames per trial from our video data. The powdering workaround for settled flows, however, limits us to a single image per trial, as the introduction of this third particle species induces instabilities and modifies the assumptions of our theoretical model.

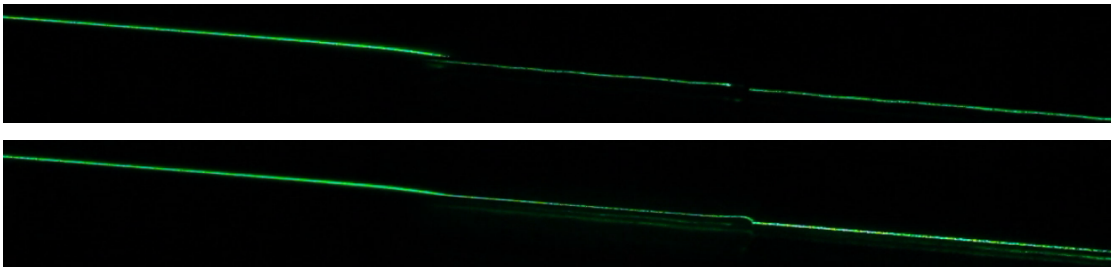

Figure 9: Top: Settled flow without powdering. Laser does not relfect off fluid. Bottom: Settled flow with powdering. Laser curvature shows two visible shocks.

3 Post-processing

3.1 Monodisperse Data

The monodisperse case is processed by converting the movie into discrete images at one frame per seconds. Then, in the code *monodisperse processor* the user is required to input the folder name containing the images, the image names, a later image, the first frame where the particle mixture passes zero, and the last frame before the mixture runs off the track. The script will prompt for the crop bounds, centimeter marks, and color from the later image. The user chooses the crop bounds so that the whole track remains within the marks. In another figure, the program will then prompt the user to select pixels of the desired color converted from RGB to HSV. The desirable later photo should show a large amount of the particle color and a sufficient amount of pixels should be chosen to get a good range for the minimum and maximum of this color. If the range does not appear large enough when the data is processed, the ranges can be manually altered to include a wider threshold of the color distribution. This information should be saved in a preprocessing 'mat' file so that the analysis can be repeated. The function *process data monocolor* will calculate the front position of the particles based on the selected color and the front position of the fluid by enhancing and comparing the present image to a later image to avoid being affected by background noise (i.e. dark spots in the background paper). In addition, the fluid front has a mask used to cover the background noise and parts of the particle front also detected by the enhancement. After the position of the fronts are detected, the y-positions are averaged to the estimate of the front position in the x-direction. This distance is converted from pixels to centimeters and then assigned to the appropriate time. These averaged front positions and time can then be used to compare to the simulations of the numerical solution from the theory.

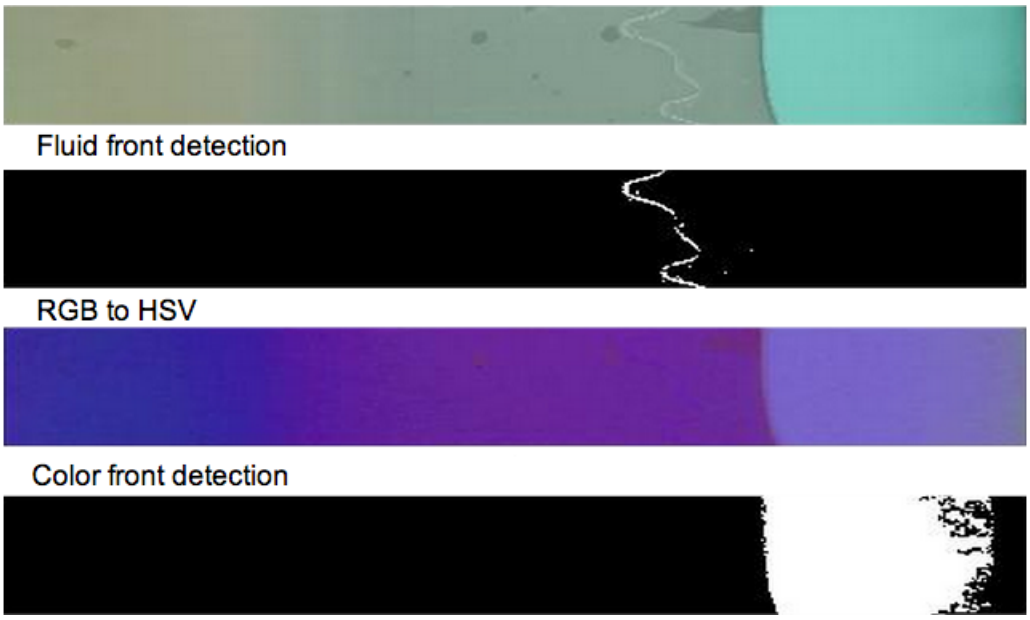

Figure 10: Edge and color detection process.

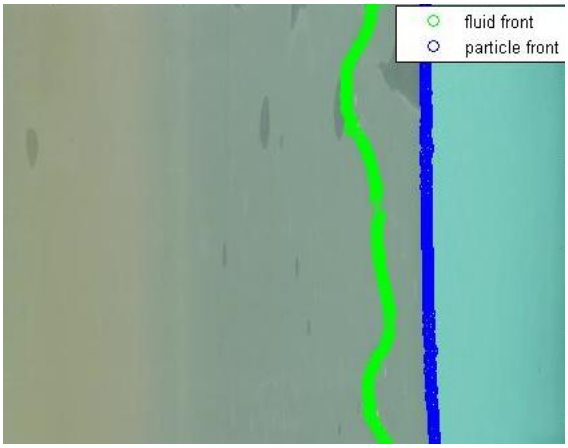

Figure 11: Position of the particle and liquid fronts.

3.2 Bidisperse Data

The bidisperse case is processed similarly to the monodisperse cases by converting the movie into discrete images at one frame per seconds. The code *bidisperse processor*, which is structurallty simiular to the code *monodisperse processor* from Section 3.1, works best to show the separation between glass and ceramic particles at $\lambda = 0.5$. The function *process data color* will calculate the front position of the red GSB particles based on the selected color and the front position of the ceramic particle by detecting the back position of the red GSB color. The front position of the fluid is obtained the same way as in the monodisperse case.

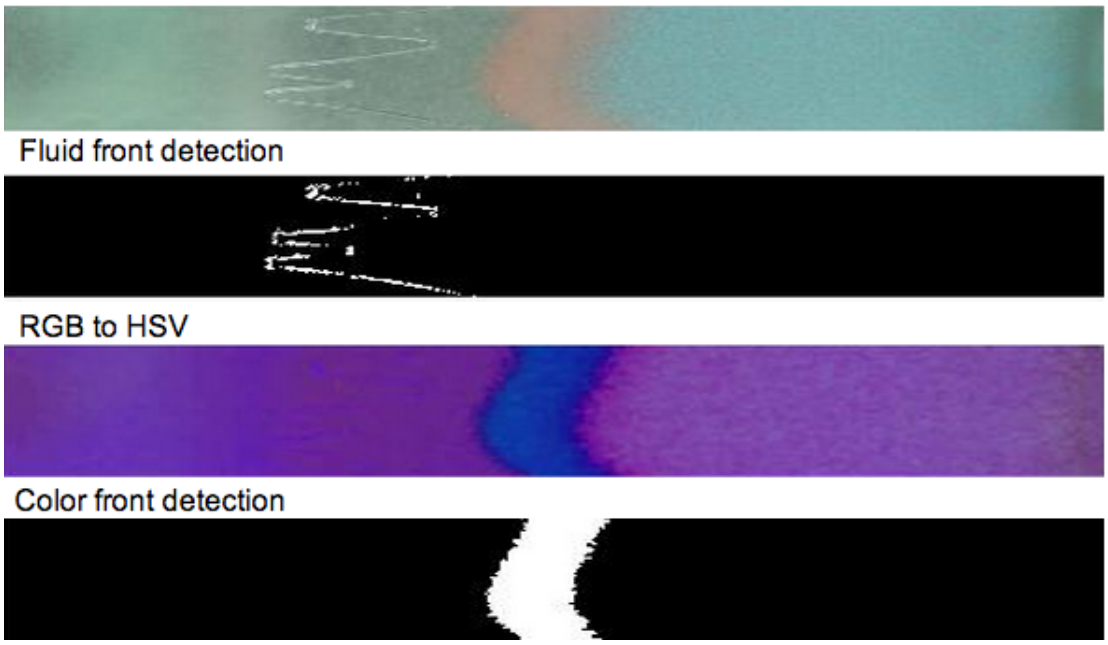

Figure 12: Edge and color detection process.

Figure 13: Position of the particle and liquid fronts.

3.3 Fluorescent Data

Before processing the fluorescent data, the calibration data must be processed. In the folder with the position and density calibration images, we open the script *caligreenGSB*. In this script, the user inputs the mass of the particles in grams from the density calibration and fills in the intensity pictures corresponding to those densities. Also, the user fills in the area of the sample used to calculate the respective particle densities. The function *fl intensity* calculates the intensity by taking the average intensities of the Petri dish area selected by the user.

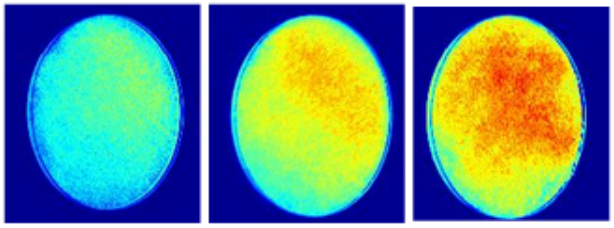

Figure 14: Density calibration.

Next, the user enters the locations of the samples in the position calibration and the names of the position sample images. In the last section, in the definition of the variable *intensity diff*, the user will need to change the value in the numerator to be the intensity value from the density calibration that corresponds to the same density used in the position calibrations. This proportion calculated will be used to convert the intensity of the sample at a particular position to the intensity of the sample placed in the center of the track ($\sim 47cm$), which then is fitted to get the density value from the first calibration. After saving the workspace of the calibration in a 'mat' file, one deletes everything except the polynomials variables *denspoly* and *pospoly*. These will be used in the assessment of the density in the experimental data. In *flu processor* script, the user will have to select a background photo with the lights on to obtain the crop bounds and the conversion of pixel to centimeter polynomial. The three polynomials and crop bounds should be saved in a preprocessing 'mat' file. In the function *flu density* implemented in this script, the user needs to put the name of the folder with the images, the image names, the first frame where the particle mixture passes the zero mark and the last frame before the particles run off the track. The code will process the data to find the density at every point and then average theses densities to get a value for every y-position. After every image is processed the integral of the density curved is calculated for each time step and saved to see in the volume remains constant. If the debugger is used, a video is created with plots of the average intensity, average density, and a picture of the particle flow scaled by intensity.

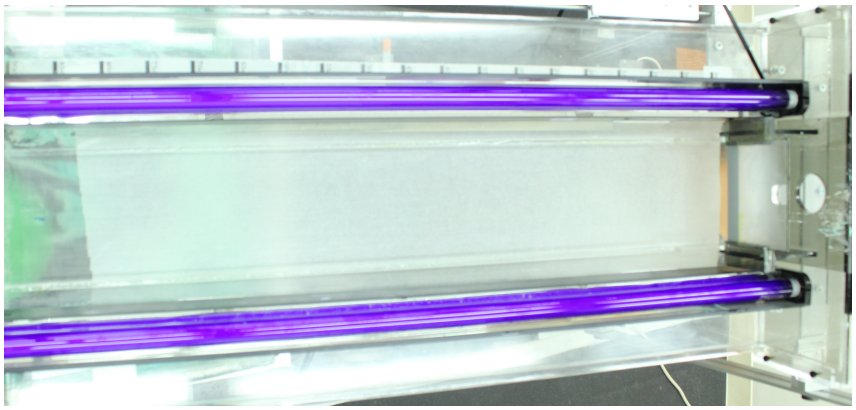

Figure 15: Background image.

3.4 Height Profile Data

For ridged and well-mixed flows, we extract the frames from our video data at specific time intervals for post-processing using several in-house MATLAB functions. This allows us to construct a time series of the height profile. In the settled regime, this is possible by performing multiple trials using an identical set of parameters and applying powder at incrementally later times. We apply Otsu's method using the built-in *graythresh* function to convert each image from RGB to binary. The threshold level varies depending on the particle-type. We achieve the best results thresholding red-dyed GSB5 particles based on the level determined by the red channel image, and undyed SLZ3 particles by the level determined by the composite image. The binary image is filtered for noise by removing connected regions that are less than 50 pixels. Operating column by column, we calculate the median value of the laser curvature (represented by 1s), and subtract this from a second-order polynomial fit on the laser baseline. These fits are approximately linear with small quadratic terms due to the bending of the track and lens barrel distortion.

The user is prompted to select the pixel position of each 5 cm marking on the ribbon to convert the position along the x-direction from pixel into centimeters. The height in pixels is normalized with respect to a polynomial fit on the ruler profile (see Fig. 8), which is of a known thickness. This corrects for the perspective of the camera angle and converts the slurry height (along the z-direction) into centimeters.

To verify our calculations, we must satisfy the requirement that the total suspension volume is conserved (see. Fig. 16). The volume for a given image is calculated by integrating the height profile over the length of the track and multiplying by the track width. To estimate the volume in regions of the incline that lie beyond the frame, we take the median slurry height and extend this value to the origin.

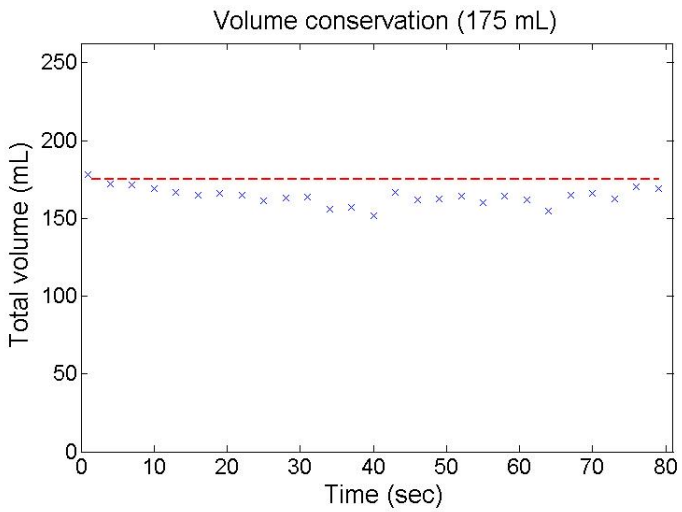

Figure 16: Experimental processes (spillage, adhesion to gate, etc.) account for volume losses. At late times, volume approximation does not exceed physical limit.

Image resolution plays a large role in post-processing. The thickness of the laser beam is comparable to the height of the slurry itself, so in order to satisfy our volume conservation criteria, we subtract off a fraction of the width of the laser line from our height profile measurement. We choose one-half to account for laser sheet scattering on the slurry surface. Uncorrected, we observe a monotonic increase in the total volume with position as it exceeds the total experimental volume, which is unphysical. Subtraction the laser half-width is a reliable technique at the current scale of our experiments; however, a more robust method is necessary to verify measurements where the laser thickness exceeds the height of the slurry.

For flows in the ridged regime, we are concerned with two additional measurements: shock width and shock height. The shock height is simply the maximum point along the height profile of the slurry. To describe the width of the shock, we calculate the full width at half max (FWHM) parameter by taking the width at half the distance from the median slurry height to the shock height (see Fig. 17). The shock width is then normalized with respect to the shock height to provide useful information about the overall shape of the shock.

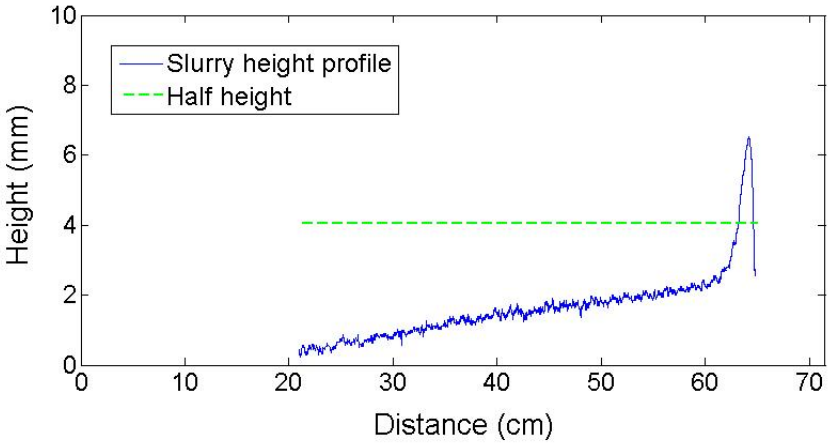

Figure 17: Width is calculated by interpolating points of intersection of height profile (discrete data set) with half max (green dotted) line.

4 Monodisperse Results

Depending on the parameters of the monodisperse experiment, we observe two kinds of outcomes: a settled or a ridged regime. The ridged regime is characterized by particles flowing down the incline without any separation from the liquid at any point along the slope. This kind of behavior is observed for combinations of large angles and higher particle concentrations (e.g. ≥ 0.4) [5]. Unlike the ridged regime, the settled regime is characterized particles settling out of the mixture, and a resulting particle front that lags behind a liquid front. This section focuses on results of this type of experiment.

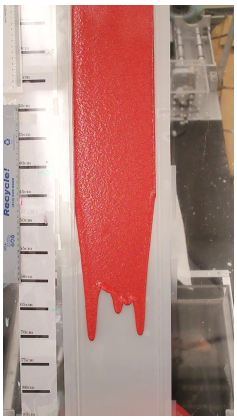

(a) Ridged Regime

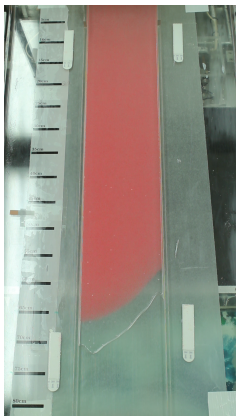

(b) Settled Regime

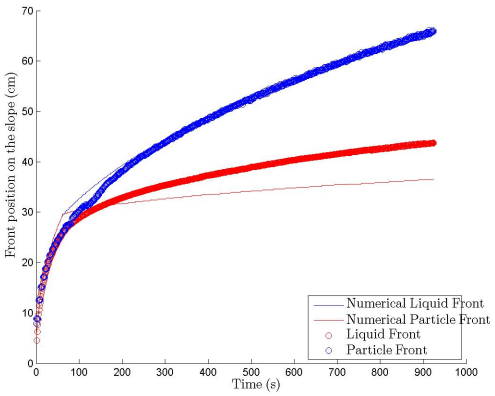

(a) GSB5: d = $\sim 0.036cm$

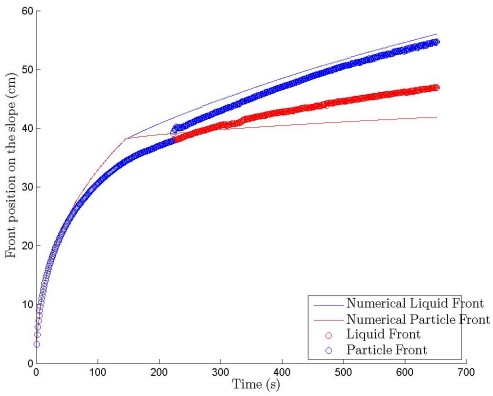

(b) GSB7: d = $\sim 0.023cm$

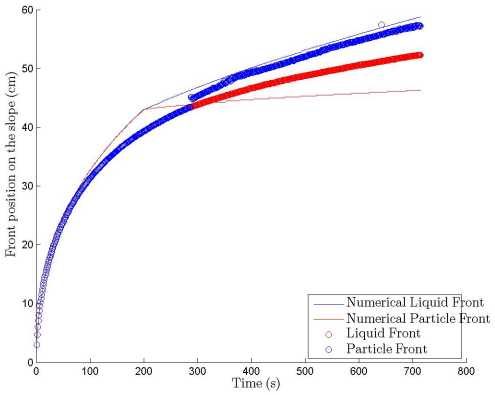

(c) GSB9: d = $\sim 0.016cm$

Figure 19: Monodisperse experiment results and numerical simulation of the solutions. Experiments depicted in (a)-(c) have parameters $\phi_0 = 0.3, \alpha = 15°$, and $V =\sim 75$ mL.

4.1 Settled Regime

In order to understand how settled bidisperse dynamics behave, we consider simpler, settled monodisperse experiments. We are focused on assessing how varying the parameters affects the length the suspension travels along the slope before there is a clear separation of particle and liquid fronts. In Figure 19, we present the comparisons for three monodisperse experiments: $\phi_0 = 0.3, \alpha = 15°$, and $V =\sim 75$ mL, for $d = 0.0360$, 0.023 and 0.016 cm. Notice that the particles and liquid separate farther along the slope as diameter decreases. In the following section we present a general theory describing the dynamics of particle settling at various experimental parameters.

4.2 Settled Regime: Transient State

4.2.1 Theory

The state during which the suspension is well-mixed is referred to as the transient state. Current numerical approximations describe the evolution of the settled regime fairly accurately, however, these approximations require the input of a transient length. One approximation for such a length is proposed by Murisic et al. [3], namely $x_{trans} = H\left(\frac{d}{H}\right)^{-2}\frac{18\rho_\ell}{\rho_p-\rho_\ell}\tan(\alpha)$. In an effort to understand this transient state better and improve upon this approximation, we propose the following approximate transient length:

$$x_{trans} = 2.7918\left(\frac{A}{d}\right)^{3/4}\left[\frac{d^3\ (\phi\ (\rho_p-\rho_\ell)\ +\rho_\ell)^3 sin^3(\alpha)}{(\rho_p-\rho_\ell)^3\ (1-\phi)^3}\right]^{1/12} \tag{1}$$

for cross-sectional area, $A = \frac{V}{w}$, volume V, width of track w, diameter of particle d, volume fraction ϕ, particle and liquid densities, ρ_p and ρ_ℓ, respectively, and angle of inclination, α.

The basis for such proposal is the following:

We assume that during the mixed state, the liquid and particles are well-mixed and behave like a Newtonian liquid. Applying Hupperts model, the mixed suspension stops abruptly at $x = x_{trans}$, where[1]

$$x_{trans} = \left(\frac{9\ A^2\ g\ sin(\alpha)}{4\ \nu}\right)^{1/3} t_{trans}^{1/3} = \left(\frac{9\ A^2\ g\ sin(\alpha)\rho(\phi)}{4\ \mu_{eff}}\right)^{1/3} t_{trans}^{1/3}, \tag{2}$$

reaching a height $h = h_{trans}$, where

[1] μ_{eff} is the effective viscosity defined as $\mu_{eff} = \mu_\ell\left(1-\frac{\phi}{\phi_M}\right)^{-2}$, where ϕ_M is the maximal packing fraction; $\rho(\phi)$ is the effective density defined as $\rho(\phi) = \phi\ (\rho_p-\rho_\ell)\ +\ \rho_\ell$

$$h_{trans} = \frac{1.5\ A}{x_{trans}}. \tag{3}$$

In order to find the time at which $x = x_{trans}$, we consider the hindered settling velocity,

$$U_{St} = \frac{g\ d^2\ (\rho_p - \rho_\ell)\ \Phi(\phi)}{18\ \mu_{eff}} = \frac{g\ d^2\ (\rho_p - \rho_\ell)\ (1-\phi)}{18\ \mu_{eff}} \tag{4}$$

The height a particle travels from the top of the suspension to the bottom is assumed to be $h = U_{St}\ t$. Thus, when the mixed state ends,

$$U_{St}\ t_{trans} = h_{trans}(t_{trans}) \tag{5}$$

or more explicitly,

$$U_{St}\ t_{trans} = \frac{1.5\ A}{x_{trans}^{1/3}\ t_{trans}^{1/3}} \tag{6}$$

Solving for t_{trans} in equation (6), we obtain the approximate time at which the transient ends,

$$t_{trans} = \left[\frac{C_0\ A\ \mu_{eff}^4}{g^4\ sin(\alpha)\ \rho(\phi)\ d^6\ (\rho_p - \rho_\ell)^3\ (1-\phi)^3}\right]^{1/4};\ \ C_0 = 8748 \tag{7}$$

and substituting this time into (2), the approximate transient length becomes the equation (1).

4.2.2 Results

As will be shown below, this new theory provides more accurate approximations to the transient length than the previous estimate. Morever, this theory has a more practical application because it eliminates the dependence on suspension height, which is difficult to measure. To compare how well this theory agrees with experiment results, we consider to what degree the results follow the power rule associated with the parameters of interest, α, V, and d. In each case, we define the end of the transient state to be when the average particle and liquid front positions differ by two centimeters, to ensure a complete separation of particles and liquid. Under this definition, we then plot the transient length relative to different measures of one type of parameter (e.g. diameter) and compare this plot to the plot of the relevant power rule.

Volume and Diameter Power Rules

The power rules associated with volume and diameter in this new theory are $V^{3/4}$ and $d^{-1/2}$, repectively. In the case of the volume power rule, we compare two types of experiments, one with GSB-5 particles (diameter $d \sim 0.016$ cm) and the other with GSB-9 particles ($d \sim 0.036$ cm). Both types of experiments were conducted with volume fraction $\phi = 0.3$, at an inclination of $\alpha = 15°$. The GSB-5 experiments in this comparison consist of volumes 75, 100, 150, and 200 mL, while the GSB-9 experiments

consist of volumes 25, 50, and 100 mL. Figure 20 shows that in the GSB-9 experiments, the experimental dependence of the transient length on the volume agrees with the theoretical depence of $V^{3/4}$. This agreement also occurs in experiments with GSB-5 for volumes $\geq$ 30 mL. We do not understand the divergence observed for volumes $<$ 30 mL in the GSB-5 experiments, however, one theory is that at smaller volumes, tension forces become stronger and affect the behavior of the suspension.

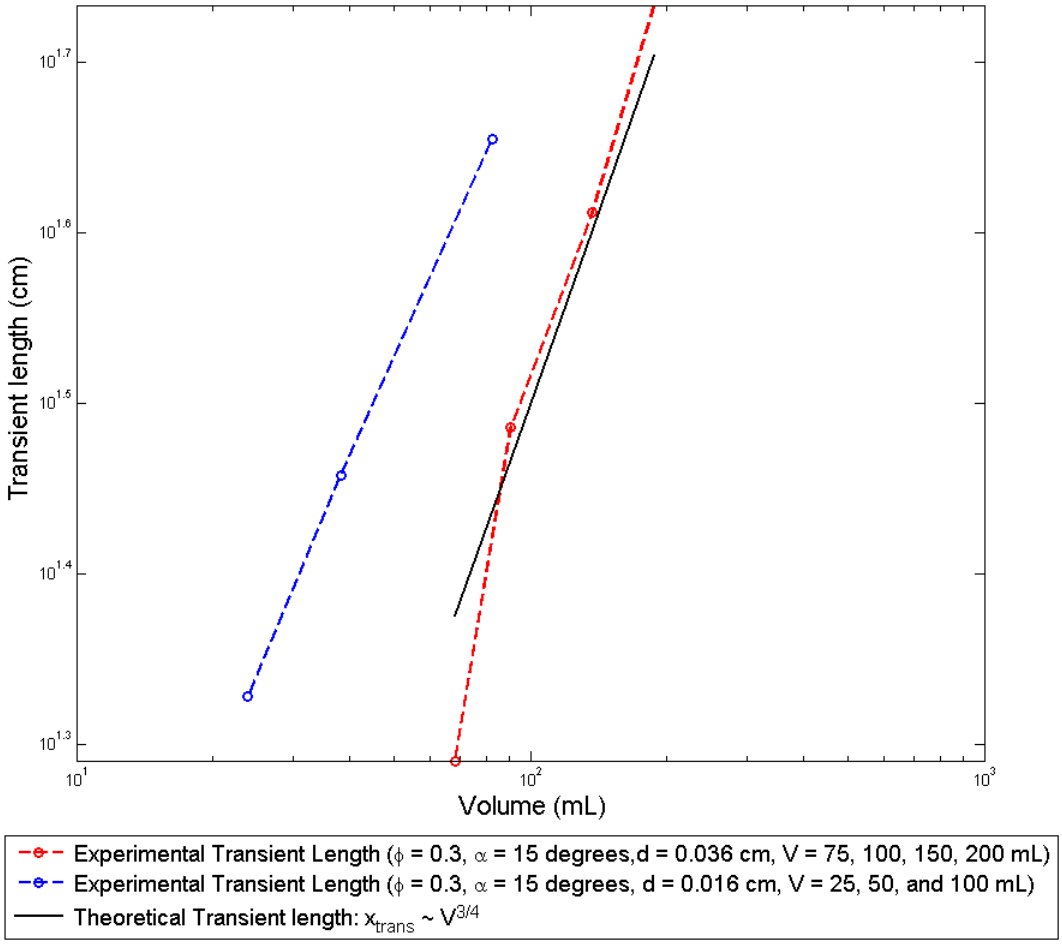

Figure 20: Experimental and theoretical comparison of volume power rule: Experiments agree with theory estimate $V^{3/4}$, for increasing volumes. Blue line consists of experiments with particle size $d = 0.016$ cm, red line consists of experiments done with $d = 0.036$ cm

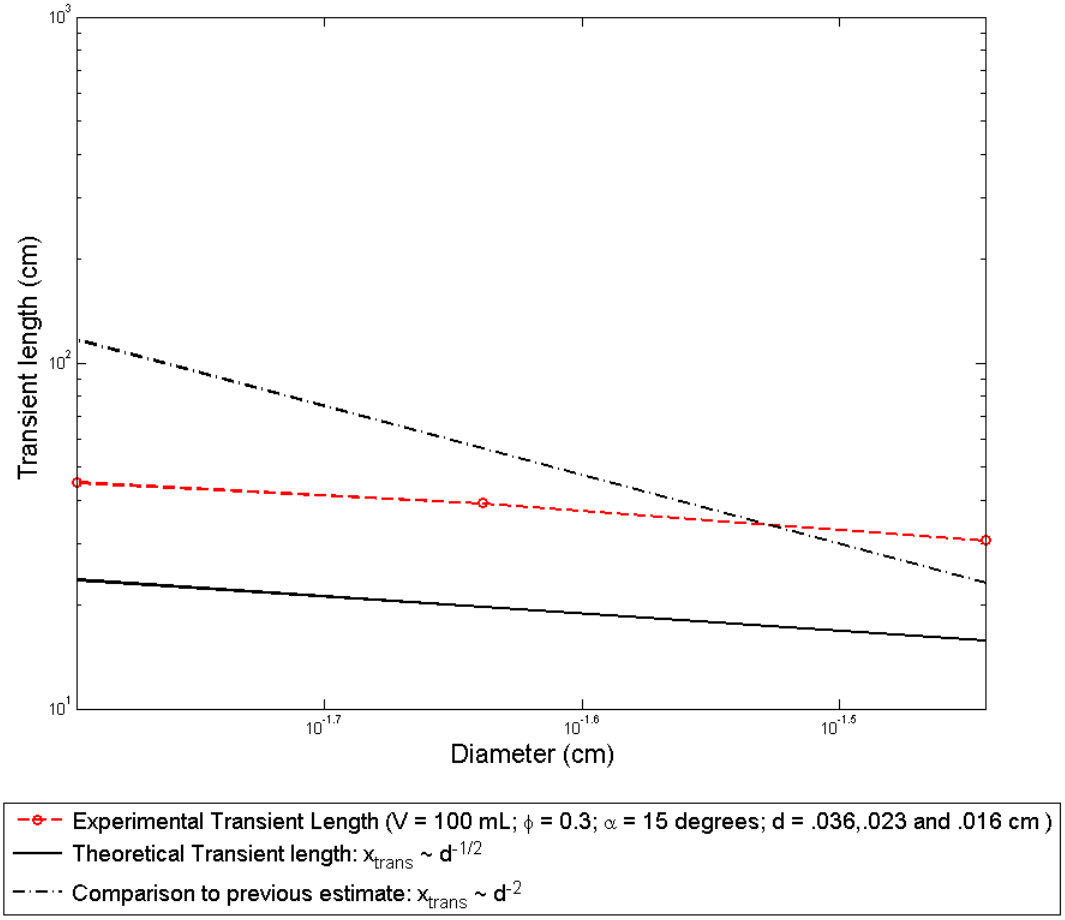

Figure 21: Experimental and theoretical comparison of diameter power rule: The experiment agrees with new theory estimate $d^{-1/2}$

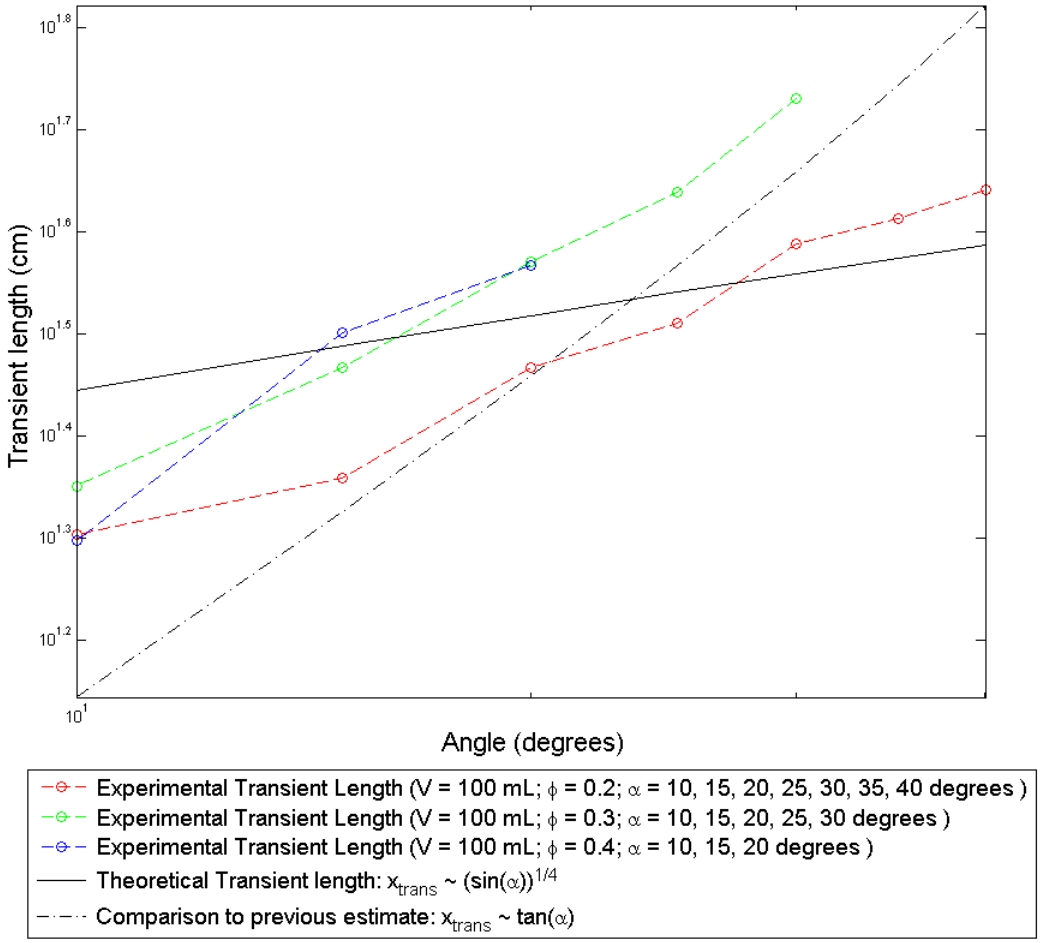

Figure 22: Experimental and theoretical comparison of angle power rule: Experimental results fluctuate, no clear agreement between theory and results.

To assess the validity of the diameter power rule, we plotted the transient lengths of experiments with particle diameters $d = 0.036, 0.023, 0.016$, where the volume was ~ 100 mL, $\phi_0 = 0.3$, and $\alpha = 15°$. Moreover, we also plotted the new and old theoretical diameter power rules $d^{-1/2}$ and d^{-2}, respectively, for comparison. In figure (21), we observe that these experiments seem to confirm the dependence $d^{-1/2}$, rather than d^{-2}. It should be noted, however, that these only constitute three points of comparison to the theory. Ideally, we should have many points for a more reliable comparison but given we only had access to particles of same density with diameters in the three ranges $.039 \pm .014$ cm (GSB-5), 0.02 ± 0.005 cm (GSB-7), and 0.03 ± 0.01 cm (GSB-9), we could only compare for these three points. For future work, it may be desireable to introduce other diameters that still satisfy the condition $\left(\frac{d}{H}\right)^2 \ll 1$ for same density particles to obtain more comparison points, or conduct the same three experiments we discussed above but with a different volume (e.g. $V = 150$ mL), in

order to further verify the theoretical estimates.

Angle Power Rule

To assess the angle power rule, $\sin(\alpha)^{1/4}$, we compare three different types of experiments carried out at 0.2, 0.3, and 0.4 volume fractions, with a total volume of ~ 100 mL. For $\phi_0 = 0.2$, we consider experiments at the angles 10°, 15°, 20°, 25°, 30°, 35° and 40°, for $\phi_0 = 0.3$, we consider experiments at $10°, 15°, 20°, 25°$ and 30°, and for $\phi_0 = 0.4$, we consider experiments at 10°, 15° and 20°. In the plot, we also consider the dependence on the angle as predicted by Bertozzi et al., $x_{trans} \sim O(\tan(\alpha))$ for comparison. As can be observed in figure (22), it appears that for $\alpha = 10°$ and 15°, the experiments with $\phi_0 = 0.2$ agree with the new theory, experiments with $\phi_0 = 0.4$ agree with the old theory, while the experiments with $\phi_0 = 0.3$ agree with neither. For $\alpha = 25°$ and 30°, the experiments with $\phi_0 = 0.3$, seem to follow the old theory, and for all other experiments, no agreement of any kind is apparent. Thus we conclude that our theory does not accurately portray the dependence of transient length on angle of inclination. One possible explanation for this may lie in the assumption that at $x = x_{trans}$, $h_{trans} = U_{st} \cdot t_{trans}$. We have assumed that a particle falls vertically from the top of the liquid to the bottom, when in reality, it falls at an angle, hence, a more realistic distance is perhaps given by $h_{trans} = U_{st} \cos(\alpha) \cdot t_{trans}$. We leave the derivation and validation of a revised transient length using this assumption for future work.

4.3 Fluorescent Data

When processing the results for the density profile, there were several issues with the fluorescent data. One of the best ways of finding discrepancies is by taking the volume for each density curve and plotting it over time and then comparing it to the expect volume. In the diagram below, the desirable volume for a solution of 0.2 particle volume fraction with initial volume of 100 mL is 20 mL and with mixture remaining after the solution is poured down the track makes the more reasonable range to be 16-20 mL. There is a red line in plot to indicated the absolute maximum volume to be 20 mL.

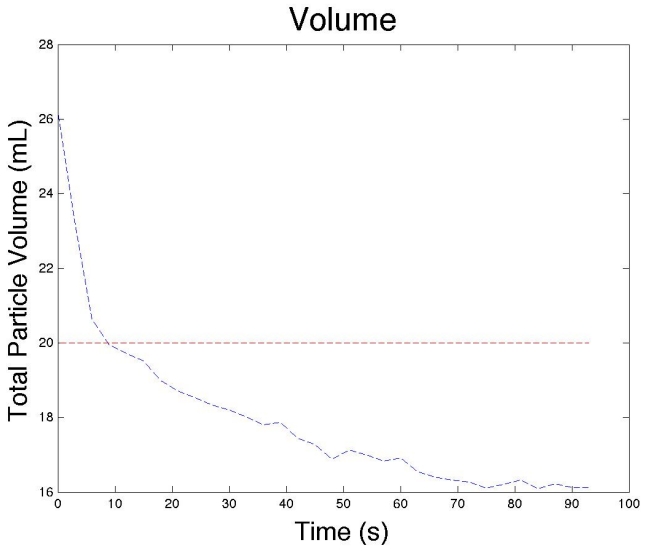

Figure 23: Total volume over time of the green GSB5 particles, particle volume fraction 0.2, initial total volume of 100mL (∼19 mL volume loss), 40 degree incline.

There should be a constant volume in this plot however the irregularity can be contributed to saturation of the particles at the beginning and the inability of the camera to detect sparse particles. From the calibration, we can see that the particle's intensities are best tested within a range of 0.04 cm - 0.11 cm. If the corresponding intensity happens to be higher than this range, a density may estimated by the polynomial fit that is not reasonable. More likely, the issue of impossibly high volume at the beginning of the experiment may be due to the scaling factor for the intensity difference making the normalized intensity too large and so the density comes out being much higher than what is expected.

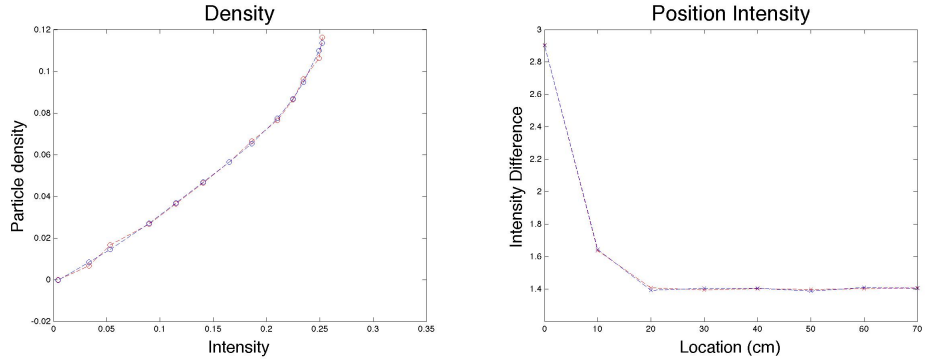

Figure 24: Density to intensity calibration (Left). Position calibration for the intensity difference (Right).

A combination of the saturation issue in the intensity to density calibration and the scale factor may be attributed to these irregularities. Also, the particles left in the gate will not be lit by the black light since the gate blocks the light from reaching them. This is likely another reason the volume is underestimate and varies with time

as particle will leave this gate area. It seems that luck and care may be a large factor in getting these experiments to work. Perhaps more samples for the calibrations would make better polynomial fits. Despite these minor issue, after comparing the results from this data to a numerical simulation for the particle density, it is apparent that the procedure and code for the density profile works well.

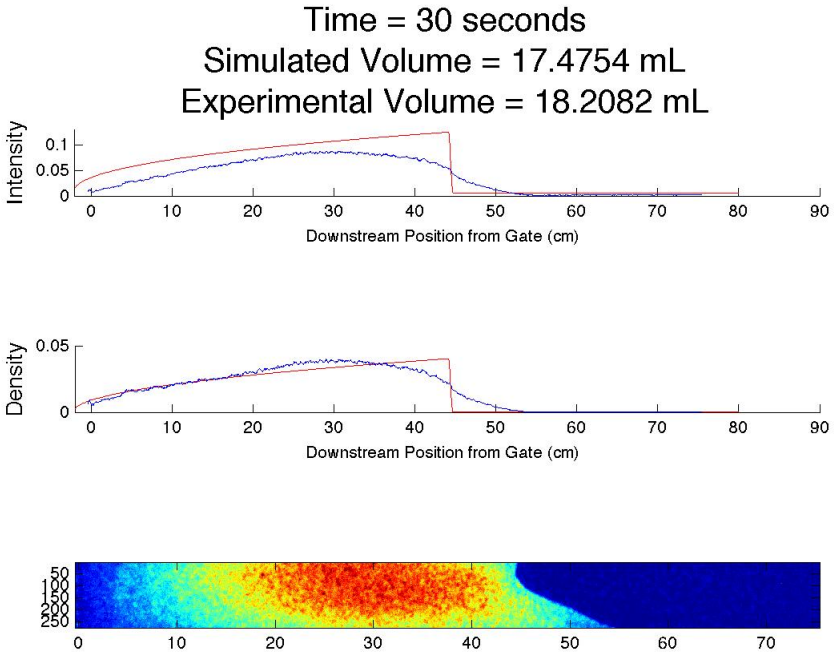

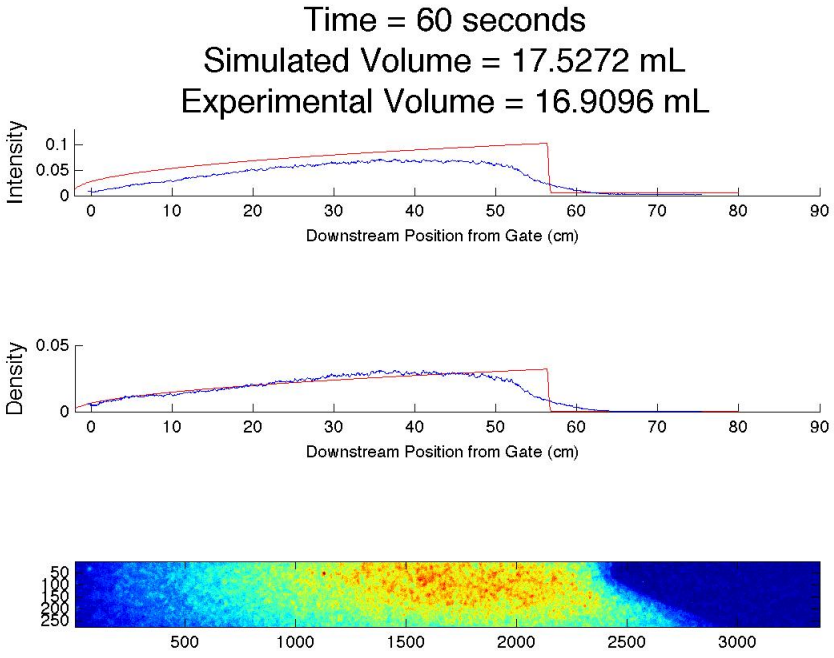

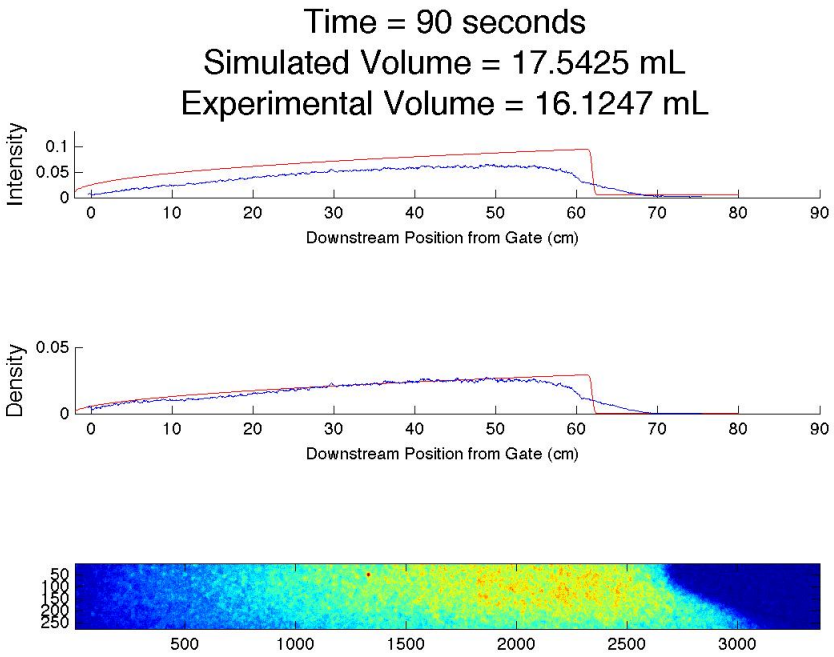

Figure 25: Green GSB5 particles, particle volume fraction 0.2, initial total volume of 100mL (∼19 mL volume loss), 40 degree incline.

These graph are from the same data used to get the total volume plot at three particular times. The blue line shown is the experimental average density calculated from the density profile which was obtained by the position scaled intensity profile. The red line was made from doing the simulation for the particle density given the parameters of the experimental regime. An inverted polynomial fit from the density calibrations was used to convert the simulated density into approximate intensities as seen in the plots. The volumes are close to the expected volume derived by taking the integral of the simulated density profile. Unfortunately, there appears to be volume loss as time increases even though none of the solution leaves the track. However, this experiment is hopeful and with the procedure properly implemented, it has been found that each time the results look more and more like the prediction. In the following sections, we present our revision of our transient theory, as well as various results for monodisperse experiments.

4.4 Height Profile Data

4.4.1 Ridged

In this section, we present results for the height profiles of particle-laden flows in the ridged regime. Particularly, we are interested in exploring the early and late time stages of shock development and collapse. Figure 26 shows time series of the height profiles for two trials at different experimental parameters. From a qualitative view, we observe the shock in the top plot sharpen as a function of time and front position.

In the bottom plot, the shock formation reaches a maximum in height before flattening toward the end of the run. This observation suggest that a shock development is overcome by factors such as surface tension with sufficient time. If we could extend our track to $200\,cm$, we might observe the shock in the top plot begin to collapse. Currently, we do not have a theory that can predict the onset of the shock flattening stage.

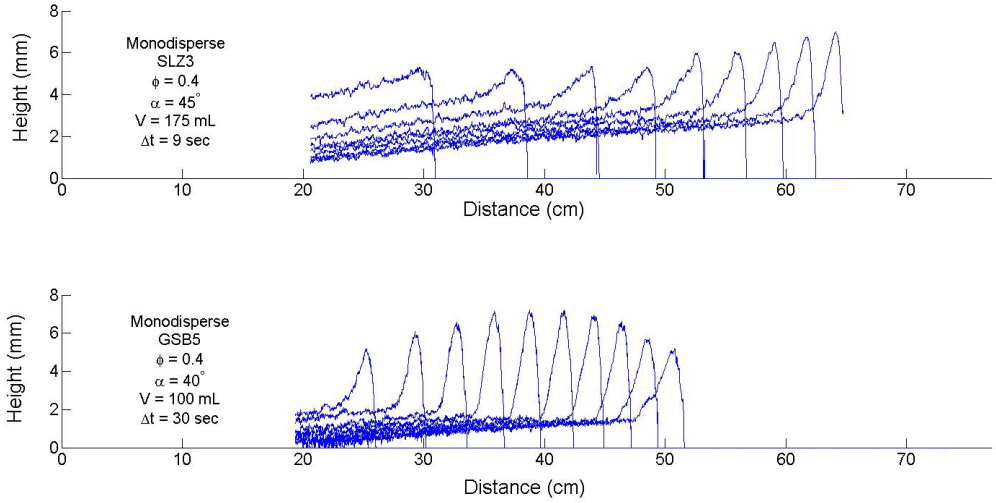

Figure 26: Plot of height profiles at regular time intervals shows shock sharpening sub-regime (top) and the onset of shock flattening sub-regime (bottom) at the length scale of our experimental setup.

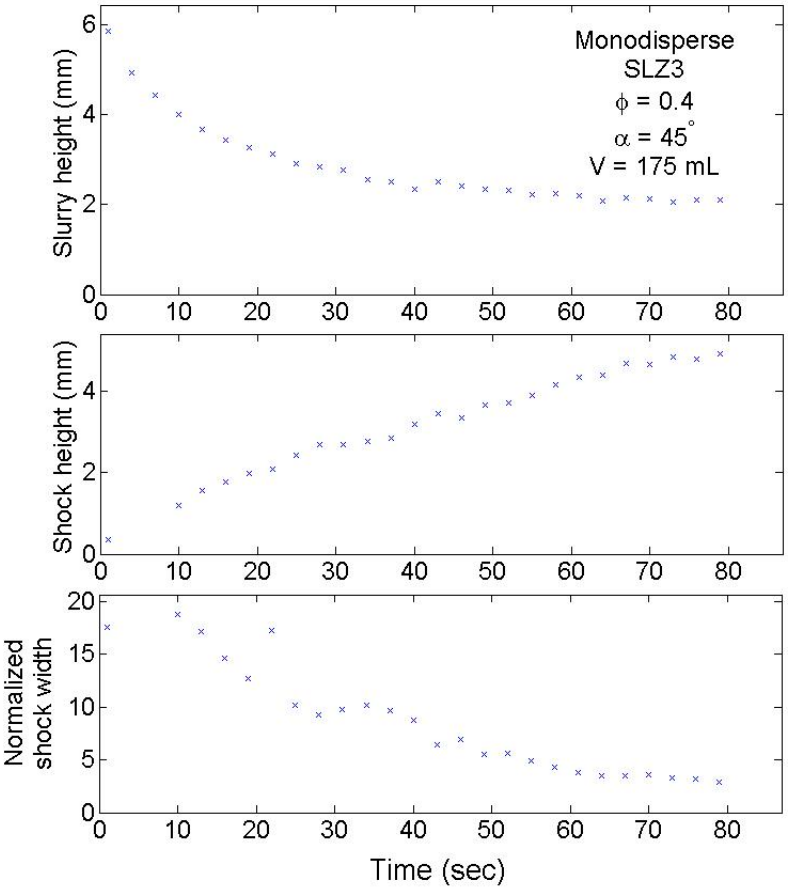

Figure 27: Plot of height profiles at regular time intervals shows onset of shock flattening at the length scale of our experimental setup.

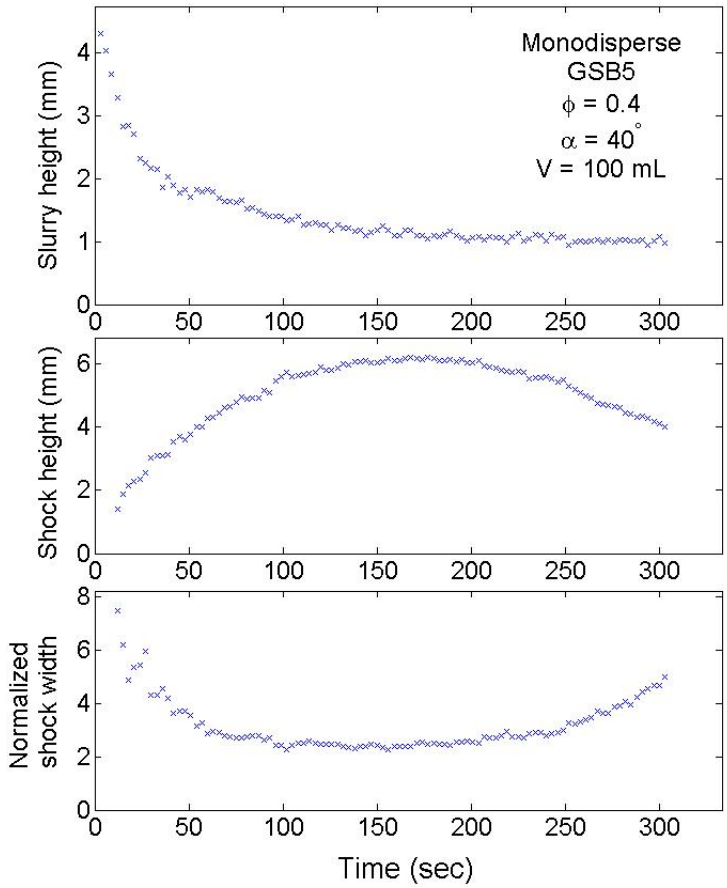

Figure 28: Plot of height profiles at regular time intervals shows onset of shock flattening at the length scale of our experimental setup.

Measurements of the shock height and normalized shock width match our previously stated observations. As expected, the median slurry height decreases as a function of time. Figure 27, which corresponds to the top plot in the previous image, shows an increasing trend in the shock height and a decreasing trend in the normalized width. In Figure 28, corresponding to the bottom time series plot, we can see that shock height reach a maximum around 175 seconds, after which it begins to decrease. The inverse is true for the shock width. Future work entails varying the parameters of our experiments in order to plot the trends in shock height maxima.

4.4.2 Settled

We restrict our discussion of the height profile for the settled regime to snapshots of flows at a well separated state. Time constraints did not allow us to construct a time series across multiple trials for any single set of parameters. However, we do present a compelling comparison of our data at single point in time to our upwind scheme simulation. Figure 29 demonstrates the predictive power of our model with regards to the jump in height at the particle shock and the advancement of the fluid

front at the exact same time scales. A natural extension of this comparison is the bidisperse settled case; initial experiments, however, do not reveal separate particle shocks for the inidividual particle species. It is unclear, even to the discernment of the human eye, whether optimization to our data acquisition methods can produce reliable to comparisons poly-disperse models.

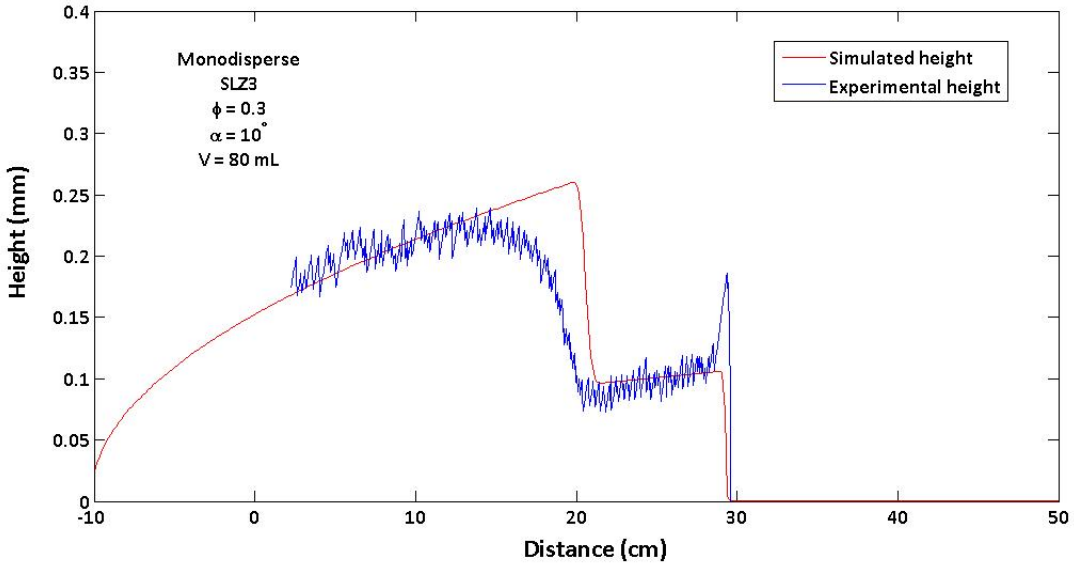

Figure 29: Comparison of experimental height profile of settled case to PDE solution; particle shock is well-predicted.

5 Bidisperse Results

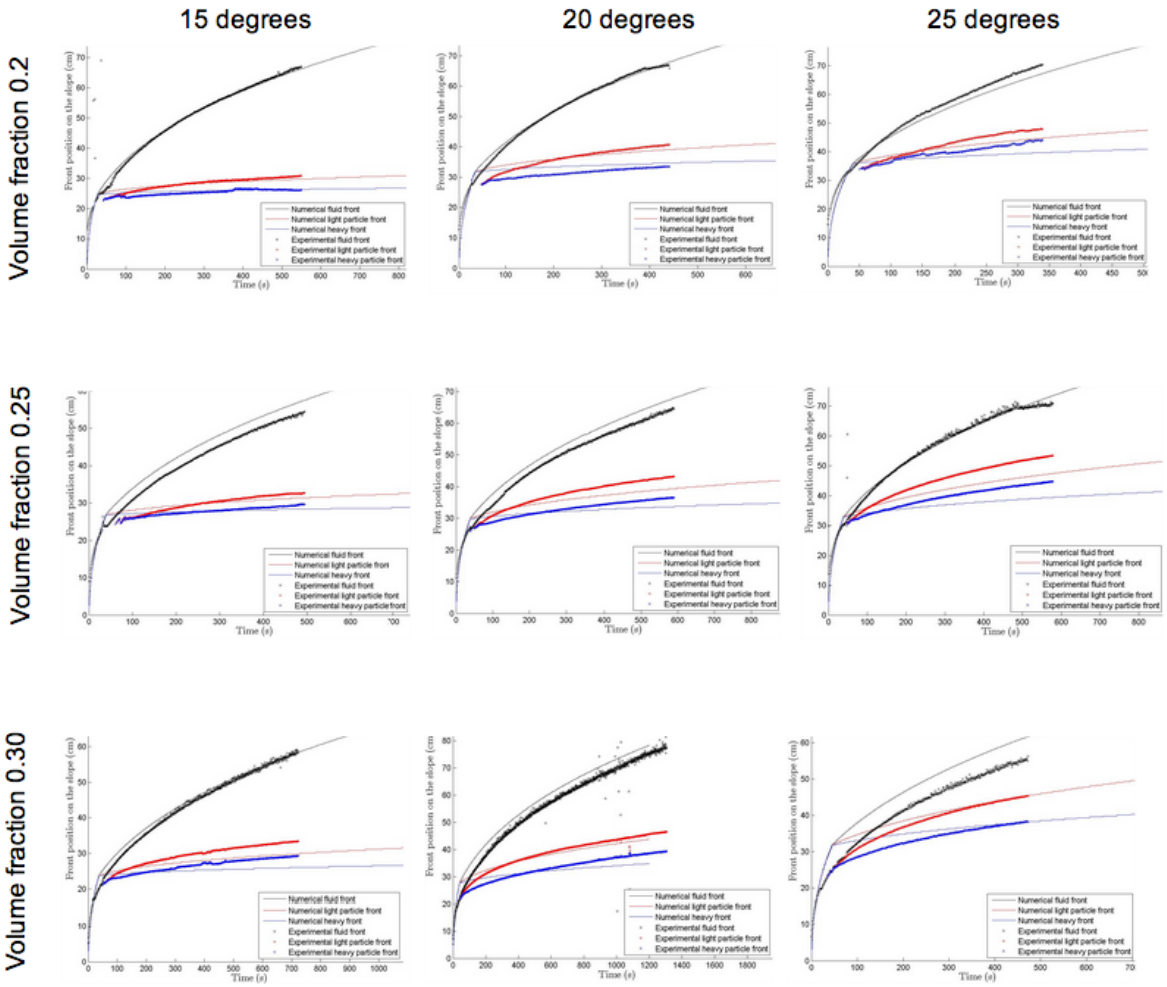

Figure 30: Bidisperse experiments with 50 % GSB 5 and 50 % Ceramic particles and 100 mL initial total volume

The results of these bidisperse experimental cases using the volume fractions of 0.2, 0.25, and 0.30 at angles 15, 20, and 25 degrees show that our understanding of the transient regime for the bidisperse case needs improvements. In the diagram, the experimental data is shown by 'x' markers with blue being the heavier particle front, red the lighter particle front, and black the fluid front. In each volume fraction regime, it appears as the angle increases the point where there are distinct fronts comes at a shorter time and at a further distance down the incline. If the angle is to remain constant and the volume fraction increases, the end of the transient comes at a shorter distance down the track and at a later time. When we compare this to the numerical simulation shown by the solid lines, it is noticeable that the simulation chooses the correct time for the end of the transient but often predicts the location of the separation to be further down the incline than where it actually

begins in the experiment. Also, for the lowest volume fraction, the pdms location in long term is well-predicted but for higher volume fractions, the front's simulated location overshoots the actual front location. For the particle fronts, the location of the particles is simulated to travel a lesser distance than its true location in the experiment and the prediction worsens as the angle increases.

6 Conclusion and Outlook

We have made advancements in the postprocessing of front behavior for bidisperse cases. Additionally, we present a revised transient theory using Huppert's model. New experimental protocol has allowed us to perform a calibration of fluorescent intensity with particle number density. However, we still encounter an issue of saturation at higher particle concentrations. We have been successful in measuring the height profile of monodisperse ridged and settled cases. Comparison of the settled case with our existing simulation yields promising results, although additional trials are necessary to verify this finding.

Future directions include matching the density measurements with height profile in order to get a concentration profile. In light of empirical evidence, we also aim to improve the dependence on α of our revised transient theory. Finally, we can compare our existing ridged height profile measurements to models that incorporate surface tension.

Acknowledgements

We would like to thank our mentors Dirk Peschka and Jeffrey Wong for their guidance and the bidisperse simulation model. We would also like to thank Professor Andrea Bertozzi, UCLA, and the NSF for providing us with this research opportunity.

References

[1] Herbert E. Huppert. Flow and instability of a viscous current down a slope. *Nature 300.5891*, 1982.

[2] David Leighton and Andreas Acrivos. The shear-induced migration of particles in concentrated suspensions. *Journal of Fluid Mechanics*, 1985.

[3] N. Murisic, B. Pausader, D. Peschka, and A. L. Bertozzi. Dynamics of paticle settling and resuspension in viscous liquid films. *Journal of Fluid Mechanics*, 2013.

[4] Thomas Ward, Chi Wey, Robert Glidden, A. E. Hosoi, and A. L. Bertozzi. Experimental study of gravitation effects in the flow of a particle-laden thin film on an inclined plane. *Physics of Fluids*, 2009.

[5] Jujie Zhou, B. Dupuy, A. L. Bertozzi, and A. E. Hosoi. Theory for shock dynamics in particle-laden thin films. *Physical Review Letters*, 2005.